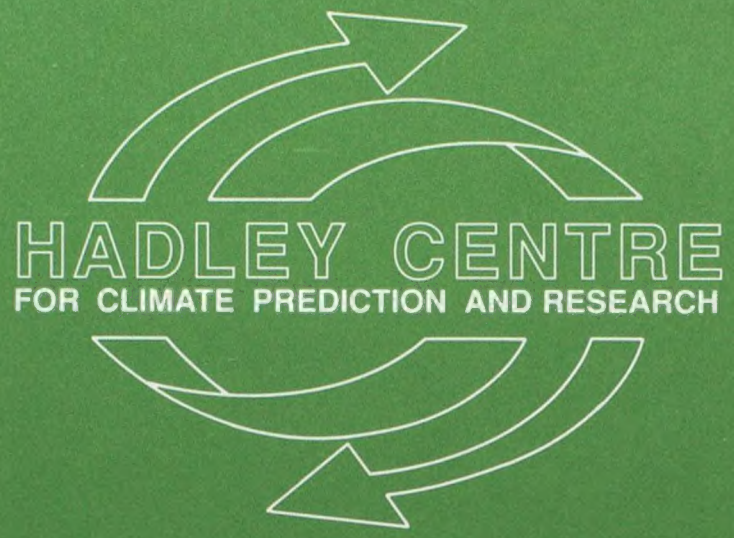

Diagnosis of dynamic sea-surface and sea-level changes from the Cox ocean model

by

J . M. Gregory

CRTN 40

September 1993

CLIMATE
RESEARCH
TECHNICAL
NOTE

Hadley Centre
Meteorological Office
London Road
Bracknell
Berkshire RG12 2SY

CLIMATE RESEARCH TECHNICAL NOTE NO.40

DIAGNOSIS OF DYNAMIC SEA-SURFACE AND SEA-LEVEL CHANGES FROM THE COX OCEAN MODEL

by

J M Gregory

Hadley Centre for Climate Prediction and Research
Meteorological Office
London Road
Bracknell
Berkshire RG12 2SY

NOTE: This paper has not been published. Permission to quote from it should be obtained from the Director of the Hadley Centre.

Diagnosis of dynamic sea-surface and sea-level changes from the Cox ocean model

The motivation for this work was an interest in extracting estimates of global and local sea-level changes under altering climatic conditions from the output of a transient coupled ocean–atmosphere experiment. This experiment (Murphy, 1992) coupled a 17-layer version of the Cox ocean model (Cox, 1984) to the Meteorological Office 11-layer atmospheric general circulation model (GCM). After 150 model years of spinup, during the final decade of which flux corrections were calculated, the coupled model was integrated for a 75-year control run and a parallel 75-year anomaly run wherein the atmospheric CO_2 concentration increased at 1% p.a., leading to a doubling after 70 years. As the atmospheric composition was not held constant, the final state of the experiment was not an equilibrium. In fact, the final globally averaged surface temperature change was +1·9 K, which should be compared with an estimated model climate sensitivity of +2·5 K.

Since the Cox model has a "rigid lid" instead of a dynamic sea-surface, it obviously does not directly give any information about sea-level or sea-surface topography. Under certain assumptions, the total change in volume of the ocean, and hence the global-average sea-level rise, can be calculated from the 3D fields of temperature and salinity using the equation of state. (In Section 5 we discuss this in greater detail.) However, changes in sea-level caused by alterations in ocean dynamics can be of the same order of magnitude, and therefore cannot be neglected if we want to obtain a map of local sea-level changes.

The sea-surface in the Cox model is constrained to be flat, by the application of a vertically downward surface pressure $p_s(x, y)$. We may suppose that this represents an extra depth $h(x, y)$ of water which would be there if the model had a free surface, and which can be calculated using the hydrostatic relation

$$p_s = h\rho g,$$

where ρ is the density and g is the acceleration due to gravity. In point of fact, as we shall see, we cannot diagnose p_s itself, but only its horizontal gradient field, and hence only the relative surface topography. However, knowing the changes both in the relative topography and in the globally averaged sea-level, we are able to obtain a map of local sea-level changes, as we set out to do. This note presents the details of the dynamical calculation, which gives the relative topography changes. On the way, we obtain some other interesting results about the Cox ocean.

1 Cox model dynamics

In the following description, equation number references are given to Cox (1984). For fields and quantities in the ocean model, cgs units are employed.

The basic equation of motion for the Cox ocean (Cox equations 3,4) is

$$\frac{\mathrm{d}\mathbf{u}_H}{\mathrm{d}t} = \frac{\partial \mathbf{u}_H}{\partial t} + \Gamma(\mathbf{u}_H) = -\mathbf{f} \times \mathbf{u}_H + \frac{1}{\rho_0}\mathbf{F} - \frac{1}{\rho_0}\nabla_H p, \tag{1}$$

where $\mathbf{u}_H$ is the horizontal velocity (composed of barotropic + baroclinic components), Γ the advection operator (Cox equation 2) ($\Gamma(\mu) = \mathbf{u}\cdot\nabla\mu$ for a scalar μ with $\mathbf{u}$ the 3D velocity), ∇_H the horizontal gradient operator and $\mathbf{f} = f\mathbf{k}$, f being the Coriolis parameter and $\mathbf{k}$ a unit vector in the vertically upward direction. Following the Boussinesq approximation, the density is taken to be a constant reference value $\rho_0 = 1$ g cm^{-3} except for the calculation of the horizontal gradient of the pressure p, which has two terms (Cox equation 5),

$$p(x, y, z) = p_s(x, y) + \int_z^0 g\rho(x, y, z')\,\mathrm{d}z' \Rightarrow \nabla_H p = \nabla_H p_s + \sigma,\ \sigma \equiv g\int_z^0 \nabla_H \rho\,\mathrm{d}z'. \tag{2}$$

Note that z is positive upwards and zero at the (fixed) surface, so that in the body of the ocean it is negative. Density ρ is calculated using the equation of state, which is represented by a parameterisation based on that of Fofonoff. The effect of pressure is included approximately in this by using different sets of coefficients dependent on model level, *i.e.* depth, but not on location, so that $\rho = \rho(T(x, y, z), S(x, y, z), p(z)) = \rho(x, y, z)$, T being temperature and S salinity.

The friction or diffusion term is separated into a horizontal part $\mathbf{F}_H$ involving a constant horizontal viscosity $D_H = 3 \times 10^9$ cm^{2}s^{-1} and a vertical part $\mathbf{F}_V$ with a stability-dependent vertical viscosity $D_V(\rho, \mathbf{u})$ (Pacanowski and Philander, 1981). The formulation of horizontal friction is obtained by applying a shallow-water approximation to the stress-strain relations for a transversely isotropic fluid (*i.e.*

one which is isotropic in one plane, the horizontal in this case). (This approximation is demonstrated by Williams (1972). Note that the horizontal terms are similar to, but *not* identical with, the two-dimensional vector Laplacian.) The surface windstress is applied as a boundary condition to the vertical diffusion term.

Putting together (1) and (2) we obtain

$$\frac{\partial \mathbf{u}_H}{\partial t} = -\Gamma(\mathbf{u}_H) - \mathbf{f} \times \mathbf{u}_H + \mathbf{F}_H + \mathbf{F}_V - \frac{1}{\rho_0}\nabla_H p_s - \frac{1}{\rho_0}\sigma,$$

which we then split into two parts (Cox equations 17–19) thus:

$$\frac{\partial \mathbf{u}_H}{\partial t} = \mathbf{a} - \frac{1}{\rho_0}\nabla_H p_s \tag{3}$$

$$\mathbf{a} = -\Gamma(\mathbf{u}_H) - \mathbf{f} \times \mathbf{u}_H + \mathbf{F}_H + \mathbf{F}_V - \frac{1}{\rho_0}\sigma. \tag{4}$$

Cox writes $\mathbf{a} = (u_t', v_t')$. It is important to realise, however, that $\mathbf{a}$ is *not* the time-derivative of any recognisable velocity; it just happens to have the dimensions of acceleration. Since p_s does not depend on depth, averaging (3) vertically yields

$$\bar{\mathbf{a}} - \frac{1}{\rho_0}\nabla_H p_s = \overline{\frac{\partial \mathbf{u}_H}{\partial t}} = \frac{\partial \bar{\mathbf{u}}_H}{\partial t} = \frac{\partial}{\partial t}\left(\frac{1}{H}\mathbf{k} \times \nabla_H \psi\right) = \frac{1}{H}\mathbf{k} \times \nabla_H \frac{\partial \psi}{\partial t}, \tag{5}$$

using the definition of the barotropic stream function ψ (Cox equation 23). The overline denotes the vertical average

$$\bar{\mu}(x, y) \equiv \frac{1}{H}\int_{-H}^{0} \mu(x, y, z)\, dz$$

(Cox equation 21), where $H(x, y)$ is the depth of the ocean.

In the prognostic equations for the ocean model, p_s is of no interest; it is the stream function tendency which is wanted. This is obtained by taking $\nabla_H \times$ (5),

$$\nabla_H \times \bar{\mathbf{a}} = \mathbf{k}\nabla_H \cdot \frac{1}{H}\nabla_H \frac{\partial \psi}{\partial t}$$

(Cox equation 25). For our purposes, however, (5) is the desired result, in the form

$$\frac{1}{\rho_0}\nabla_H p_s = \bar{\mathbf{a}} - \frac{1}{H}\mathbf{k} \times \nabla_H \frac{\partial \psi}{\partial t}, \tag{6}$$

or in components

$$\frac{1}{\rho_0}\frac{\partial p_s}{\partial x} = \bar{a}_x + \frac{1}{H}\frac{\partial^2 \psi}{\partial y\, \partial t} \qquad \frac{1}{\rho_0}\frac{\partial p_s}{\partial y} = \bar{a}_y - \frac{1}{H}\frac{\partial^2 \psi}{\partial x\, \partial t}.$$

To evaluate $\nabla_H p_s$, we thus need the time derivative of the stream function and the vertical average of (4). The latter requires fields of velocity, T and S (to calculate density) and windstress τ (for the boundary conditions on $\mathbf{F}$). The total horizontal velocity $\mathbf{u}_H = \mathbf{u}_c + (\mathbf{k}/H) \times \nabla_H \psi$, where $\mathbf{u}_c$ is the horizontal baroclinic velocity. The vertical velocity is calculated by continuity, $\nabla \cdot \mathbf{u} = 0$ (constant ρ from the Boussinesq approximation). To perform the calculation, the fields required from the model are ψ, T, S, τ and $\mathbf{u}_c$.

In the model, the routine `CLINIC` calculates $\mathbf{a}$. For the purpose of this investigation, a modified version of `CLINIC` was prepared, whose inputs are fields of ψ, $\partial\psi/\partial t$, $\mathbf{u}_c$, T, S, τ and $1/H$ and which computes $\nabla_H p_s$. The vector field inputs are on the UV grid, the scalars on the TS grid (Figure 1). The modified `CLINIC` has the following stages: (1) Compute the grid spacings and other constants dependent on the grid; (2) Compute total velocity from barotropic and baroclinic parts; (3) Calculate $\mathbf{a}$ by summing the terms of (4), which we shall refer to as advection, Coriolis, horizontal and vertical diffusion and hydrostatic pressure. The model itself calculates these quantities row by row, but the modified `CLINIC` accepts and computes complete fields; (4) Calculate $\bar{\mathbf{a}}$ and $(\partial/\partial t)\nabla_H \psi$. Combine them to obtain $\nabla_H p_s$ on the UV grid. More details about the output appear in the next section. At this final stage, the results are converted to SI units.

For the time derivative of the stream function, we use a first-order estimate

$$\frac{\partial \psi}{\partial t} = \frac{\psi(t + \Delta t) - \psi(t)}{\Delta t}.$$

This obtains a field applicable to time $t + \frac{1}{2}\Delta t$, and all other quantities are made consistent with this by taking the means of fields at t and $t + \Delta t$. We use $\Delta t = 1$ a (a=year), all fields being annual averages. It is obviously necessary to think about the choice of time interval, because the advection and vertical diffusion terms in (4) are non-linear, and would therefore be generally underestimated by averages over long periods. In order to investigate the importance of this, a comparison was made between a calculation based on pair of consecutive years and the average of the results of 23 separate calculations based on pairs of consecutive months covering the same period. As expected, all the linear terms are the same in the two cases, to within 1%. In the upper levels, the vertical diffusion term is considerably larger—up to twice the size—in the monthly calculation, but as most of the windstress is absorbed near the surface (see below), this term is insignficant in much of the column, and the depth-average, which is the important quantity, is less than 1% greater. The advection is larger at all levels, and by 30% in the depth-average, but this is the smallest term anyway by a couple of orders of magnitude. As will be seen, the dominant terms are linear, and in any case the variability of the ocean is relatively small (at least on these time scales).

2 Relative surface topography

In the above result, p_s appears only as its horizontal gradient $\nabla_H p_s$. Since the gradient of a constant is zero, the gradient field will allow us to determine p_s only to within an arbitrary additive constant. Thus, we will obtain the relative, but not the absolute, surface topography.

For any scalar ϕ, $\nabla_H \times \nabla_H \phi = 0$. Hence, if $\nabla_H \times \nabla_H p_s$ does not vanish everywhere, we will not be able to find a satisfactory scalar field p_s. In practice, owing to inaccuracy of computation, $\nabla_H p_s$ will indeed not be exactly irrotational. Therefore we use a numerical minimisation to obtain an approximation to p_s.

The program utilises the NAG library routine **F04QAF** (Numerical Algorithms Group, 1990) to find an appropriate solution by a least-squares method. Given a sparse $m \times n$ matrix A and an m-element vector b, the routine finds an n-element vector q such that $r^{\mathrm{T}} r$ is minimised, where $r_k = b_k - b'_k$, $b'_k = \sum_l A_{kl} q_l$. In this application, A is a spatial finite-difference operator acting on the surface pressure field contained in q. Since the algorithm works best if the elements of A are of comparable size, we take the b to be surface pressure differences [Pa] between adjacent grid points, so that the A are all of order unity [dimensionless]. The possibly more obvious choice would be to set the b to surface pressure gradients [Pa m^{-1}], making the A reciprocal distances [m^{-1}]. In this case, the A would be much smaller at the equator than at the poles.

To describe the application in more detail, we refer to Figure 1, which gives the indices for points on the TS (t) and UV (u) grids. One element of $q = p_s$ is assigned for all TS points which are adjacent to at least one active UV point. Two elements of b are defined for each active UV point, being $b_x(i,j) = \Delta x\, \partial p_s/\partial x$, $b_y(i,j) = \Delta y\, \partial p_s/\partial y$, where $\Delta x, \Delta y$ are the dimensions of the UV box. The problem is thus overconstrained, in that there are probably around twice as many b as q. Corresponding to the b we calculate the b' thus:

$$b'_x(i,j) = q(i+1, j+\tfrac{1}{2}) - q(i, j+\tfrac{1}{2}) = \tfrac{1}{2}(q(i+1,j+1) + q(i+1,j) - q(i,j+1) - q(i,j))$$
$$b'_y(i,j) = q(i+\tfrac{1}{2}, j+1) - q(i+\tfrac{1}{2}, j) = \tfrac{1}{2}(q(i+1,j+1) - q(i+1,j) + q(i,j+1) - q(i,j)).$$

Thus for each b there are four non-zero elements of A, all with values of $\pm\frac{1}{2}$, in summary

$$A(x,i,j;i+1,j+1) = +\tfrac{1}{2} \quad A(x,i,j;i+1,j) = +\tfrac{1}{2} \quad A(x,i,j;i,j+1) = -\tfrac{1}{2} \quad A(x,i,j;i,j) = -\tfrac{1}{2}$$
$$A(y,i,j;i+1,j+1) = +\tfrac{1}{2} \quad A(y,i,j;i+1,j) = -\tfrac{1}{2} \quad A(y,i,j;i,j+1) = +\tfrac{1}{2} \quad A(y,i,j;i,j) = -\tfrac{1}{2},$$

where the notation $A(c,k,l;m,n)$ means the element of A which relates $b_c(k,l)$ to $q(m,n)$.

The algorithm also requires the transpose A^{T}. This involves considering which b' depend on a given $q(i,j)$. From Figure 1 it can be seen that q will be required for (b'_x, b'_y) at each of the four surrounding UV points. Consideration of A above shows that for each q there will be eight non-zero elements of A^{T}, as follows:

$$A^{\mathrm{T}}(i,j;x,i-1,j-1) = +\tfrac{1}{2} \quad A^{\mathrm{T}}(i,j;x,i-1,j) = +\tfrac{1}{2} \quad A^{\mathrm{T}}(i,j;x,i,j-1) = -\tfrac{1}{2} \quad A^{\mathrm{T}}(i,j;x,i,j) = -\tfrac{1}{2}$$
$$A^{\mathrm{T}}(i,j;y,i-1,j-1) = +\tfrac{1}{2} \quad A^{\mathrm{T}}(i,j;y,i-1,j) = -\tfrac{1}{2} \quad A^{\mathrm{T}}(i,j;y,i,j-1) = +\tfrac{1}{2} \quad A^{\mathrm{T}}(i,j;y,i,j) = -\tfrac{1}{2}.$$

In the program, computation of A and A^{T} is performed by **PSMATX**, which is supplied as an external to **F04QAF**. As a check on the accuracy of the numerical solution, the calculated pressure field p_s is

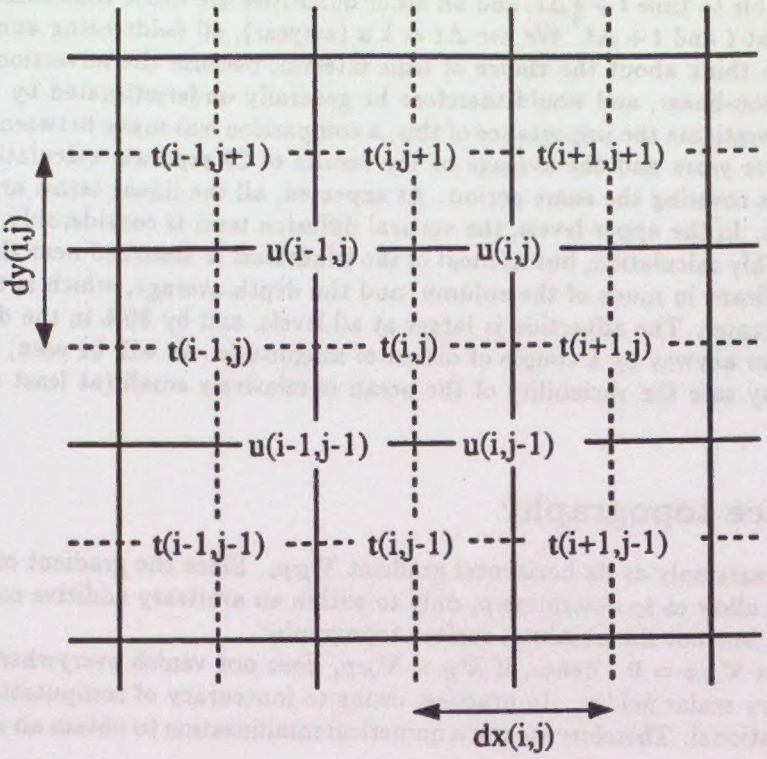

Points on the TS grid are denoted by t, on the UV grid by u.

Figure 1: Points and spacings on the horizontal TS and UV grids

redifferentiated, and the result compared with $\nabla_H p_s$. Over 92% of the ocean area, the magnitude of the new vector field is within 10% of $|\nabla_H p_s|$. Over 97%, it is within 20%, and the remaining 3% are scattered patches.

3 Results from the control simulation

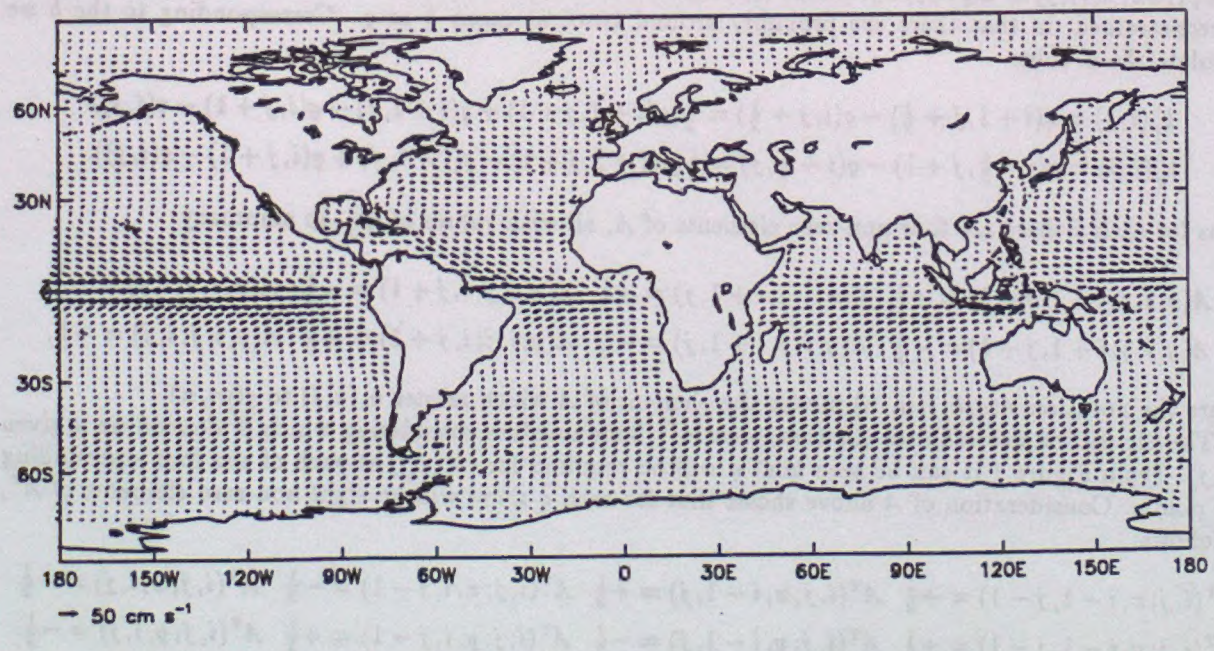

Figure 2: Top-layer velocity $\mathbf{u}_H$

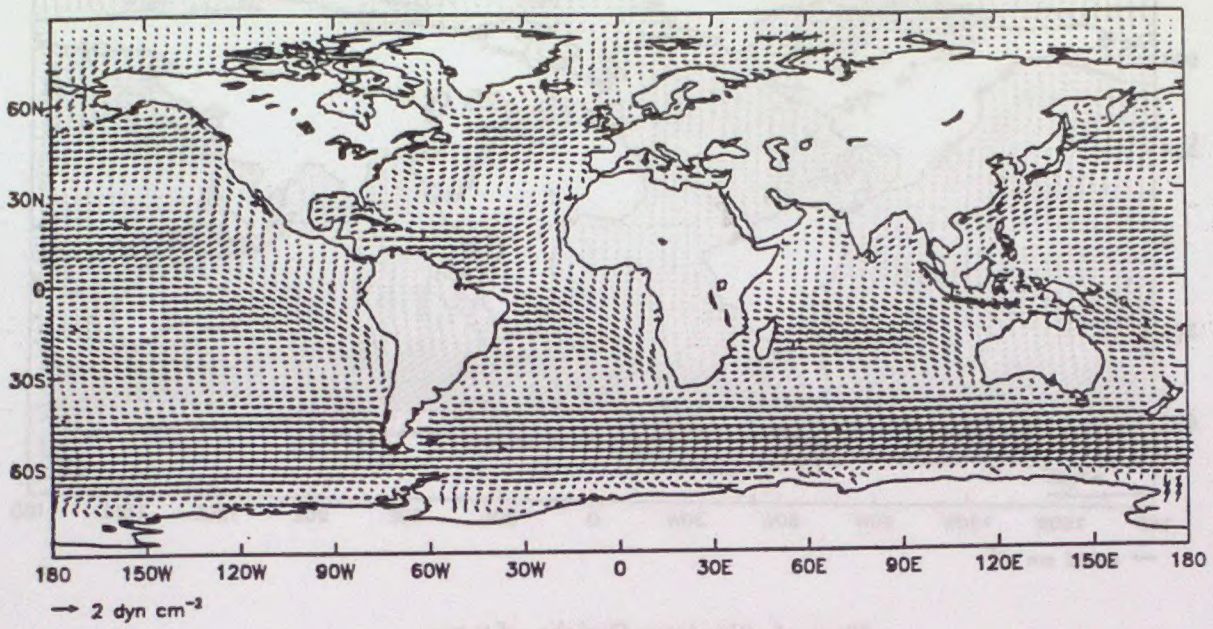

Figure 3: Surface windstress τ

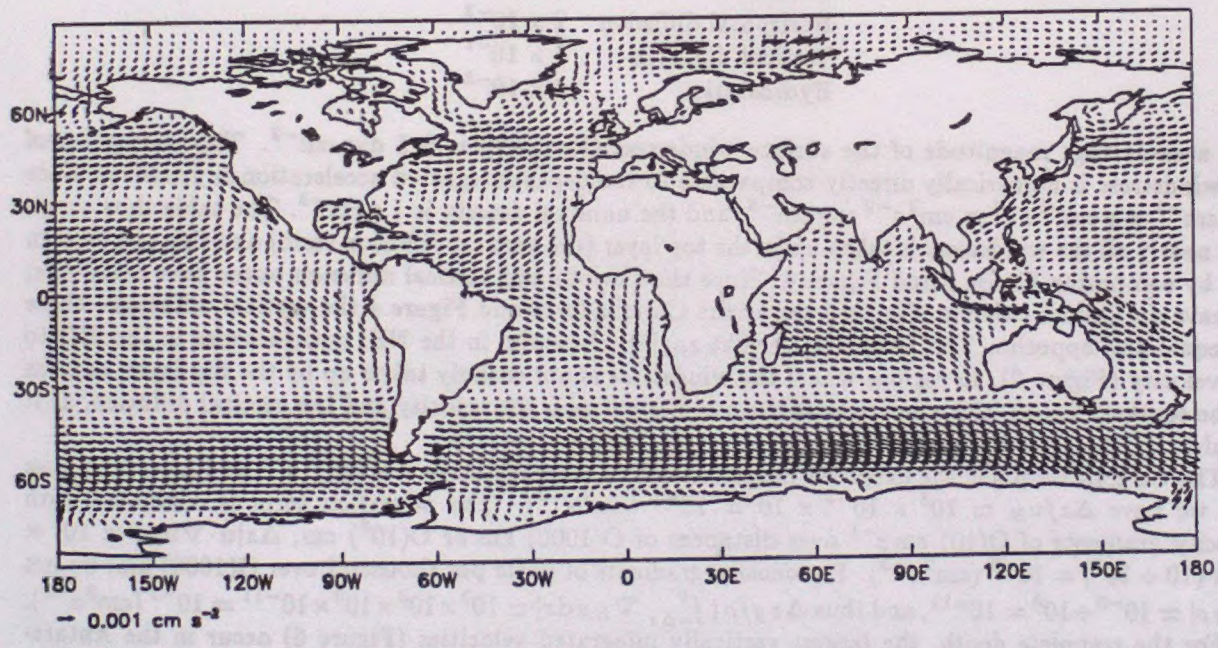

Figure 4: Top-layer vertical diffusion $D_V \partial^2 \mathbf{u}_H / \partial z^2$

As a typical example, we examine the results calculated from the first two years of the control simulation. (The calculation involves $\partial\psi/\partial t$ obtained from the annual averages of ψ for years 1–2, so the result may be taken to apply to the end of year 1.)

The surface velocity field appears in Figure 2. The largest speeds are to be found in the equatorial region, with values of a few times 10 cm s^{-1}, the area-average being 9·9 cm s^{-1}. ("Area averages" are area-weighted means over the global ocean.) The area-average values of the various acceleration terms integrated through the top layer (*n.b. integrated*, not averaged), which has a thickness of 10 m or 1000 cm, are as follows, in cm^2 s^{-2}:

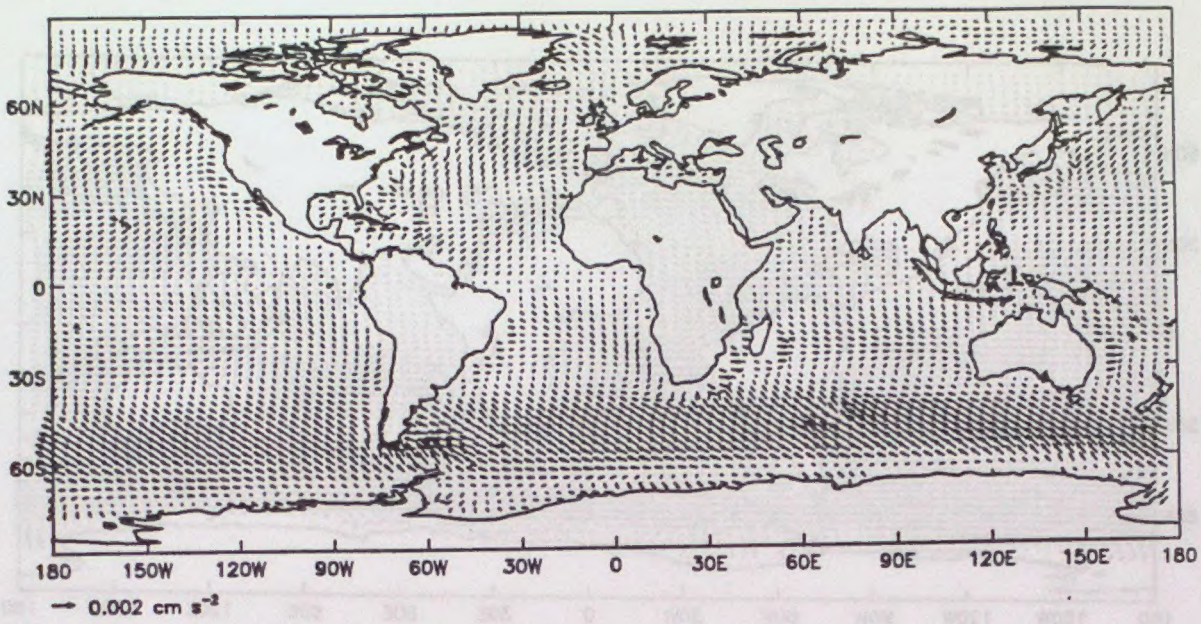

Figure 5: Top-layer Coriolis $-\mathbf{f} \times \mathbf{u}_H$

Advection	1×10^{-3}
Coriolis	5×10^{-1}
Horizontal diffusion	2×10^{-2}
Vertical diffusion	5×10^{-1}
Hydrostatic	4×10^{-3}

The area-average magnitude of the surface windstress (Figure 3) is $0{\cdot}6$ dyn cm^{-2}. The absorption of the windstress is numerically directly comparable to the depth-integrated acceleration it produces, since dyn cm^{-2} = g cm^{-1} s^{-2} = cm^2 s^{-2} × g cm^{-3}, and the nominal density is 1 g cm^{-3}. The table thus shows that nearly all the windstress is taken up in the top layer (the vertical diffusion term) and this can be seen also by comparing Figure 3 and Figure 4. Since the Coriolis and vertical diffusion terms have equal size, we have an Ekman balance. Figure 5 shows the Coriolis force and Figure 4 the vertical diffusion—these are equal and opposite. The former is at right-angles (clockwise in the NH, anticlockwise in the SH) to the velocity (Figure 2). In regions where the windstress is not entirely taken up by the top layer, such as in the southern ocean, the windstress (Figure 3) lies between the velocity and the vertical diffusion, as it should.

The Coriolis term has the expected magnitude; for a representative $f \sim 10^{-5}$ s^{-1} and layer thickness Δz, we have $\Delta z f u_H \simeq 10^3 \times 10^{-5} \times 10 = 10^{-1}$ (cm^2 s^{-2}). The advection term is consistent with velocity gradients of O(10) cm s^{-1} over distances of O(1000) km or O(10^8) cm, $\Delta z |\mathbf{u} \cdot \nabla \mathbf{u}_H| \simeq 10^3 \times 10 \times (10 \div 10^8) = 10^{-3}$ (cm^2 s^{-2}). For density gradients of parts per thousand over O(1000) km, we get $|\nabla_H \rho| \simeq 10^{-3} \div 10^8 = 10^{-11}$, and thus $\Delta z\, g/\rho \left| \int_{-\Delta z}^{0} \nabla_H \rho \, dz \right| \simeq 10^3 \times 10^3 \times 10^3 \times 10^{-11} = 10^{-2}$ (cm^2 s^{-2}).

For the complete depth, the largest vertically integrated velocities (Figure 6) occur in the Antarctic circumpolar current, and in particular through the Drake Passage, where they have magnitude $\left| \int_{-H}^{0} \mathbf{u}_H \, dz \right| = \mathrm{O}(10^6)$ cm^2 s^{-1}. This means the total transport across a line of length 100 km = 10^7 cm is 10^{13} cm^3 s^{-1} = O(10) Sv, as expected.

The area-average depth-integrated acceleration terms are as follows, in cm^2 s^{-2}:

Advection	5×10^{-3}
Coriolis	$1 \times 10^{+1}$
Horizontal diffusion	3×10^{-1}
Vertical diffusion	6×10^{-1}
Hydrostatic	$6 \times 10^{+1}$

The depth- and area-average speed is $0{\cdot}7$ cm s^{-1}, two orders of magnitude smaller than the average surface speed. Hence it is reasonable that the advection and horizontal diffusion terms are only one and two orders of magnitude larger, respectively, than their values in the surface layer, even though the full

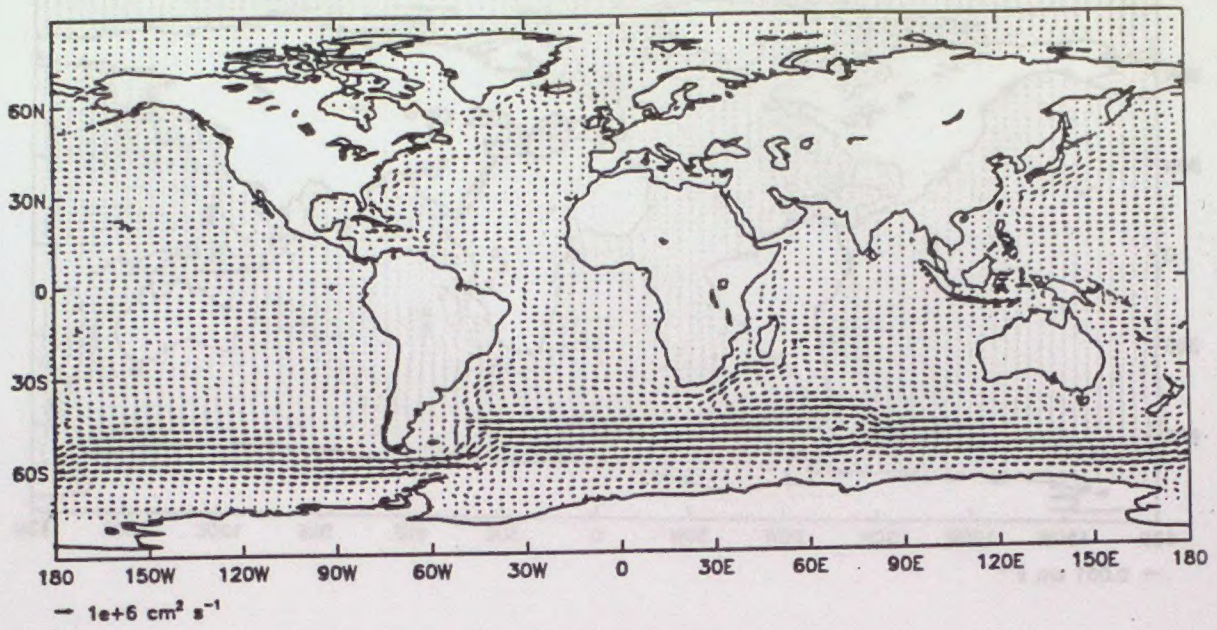

Figure 6: Depth-integrated velocity $\int_{-H}^{0} \mathbf{u}_H \, dz$

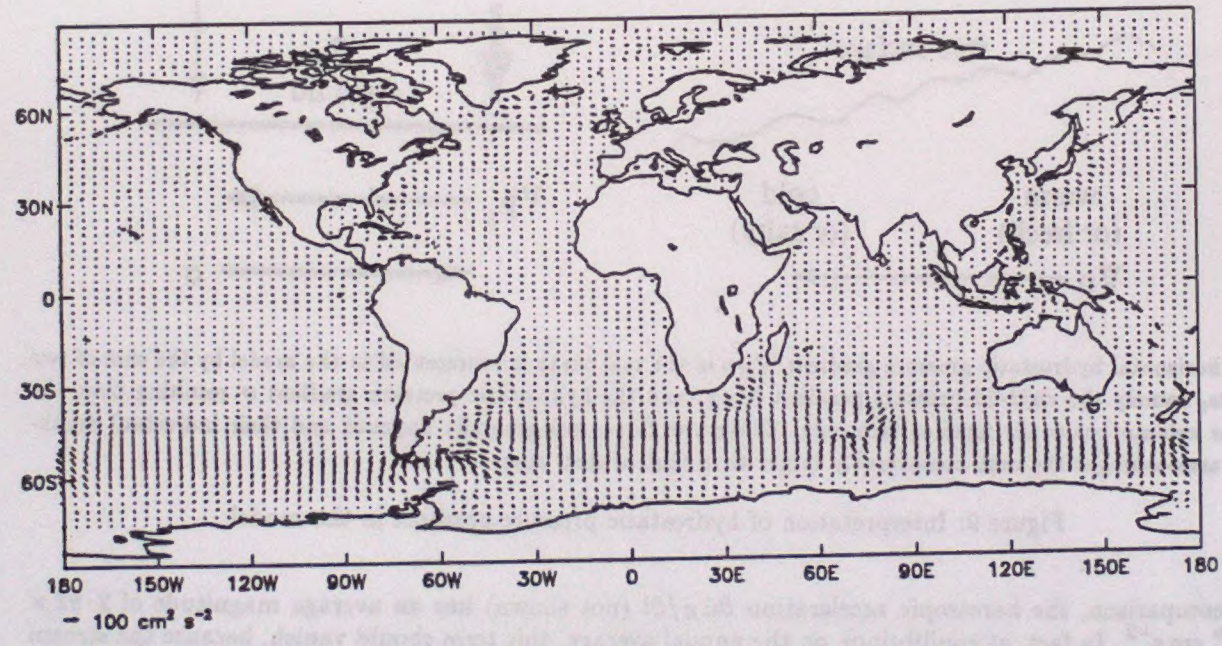

Figure 7: Depth-integrated Coriolis $-\mathbf{f} \times \int_{-H}^{0} \mathbf{u}_H \, dz$

depth is three orders of magnitude greater. Both are still negligible, even though the horizontal diffusivity has an unphysically large value. The vertical diffusion term matches the total windstress—none of the windstress is transmitted to the bottom of the ocean. A map of this quantity is exactly like that of the windstress (Figure 3). The Coriolis term, like the total volume transport, is O(100) times larger than its value for the surface layer. Inspection of Figure 7 shows that it is strongest in the Antarctic circumpolar current, where it is northwards, 90° to the left of the westward current.

The largest term for the total depth is the horizontal hydrostatic pressure gradient σ. It is important to keep in mind what this term means, recalling (2). This is *not* identical with the horizontal pressure gradient $\nabla_H p$ that exists in the real ocean, because of the rigid lid. The real $\nabla_H p$ is the *sum* of the Cox hydrostatic term σ and $\nabla_H p_s$, the quantity we are aiming to extract, and which results from the depth-average $\bar{\mathbf{a}}$ of the baroclinic terms in the above table combined with the barotropic acceleration. The baroclinic component $\bar{\mathbf{a}}$ is shown in Figure 8, and its area-average magnitude is $2{\cdot}34 \times 10^{-4}$ cm s^{-2}.

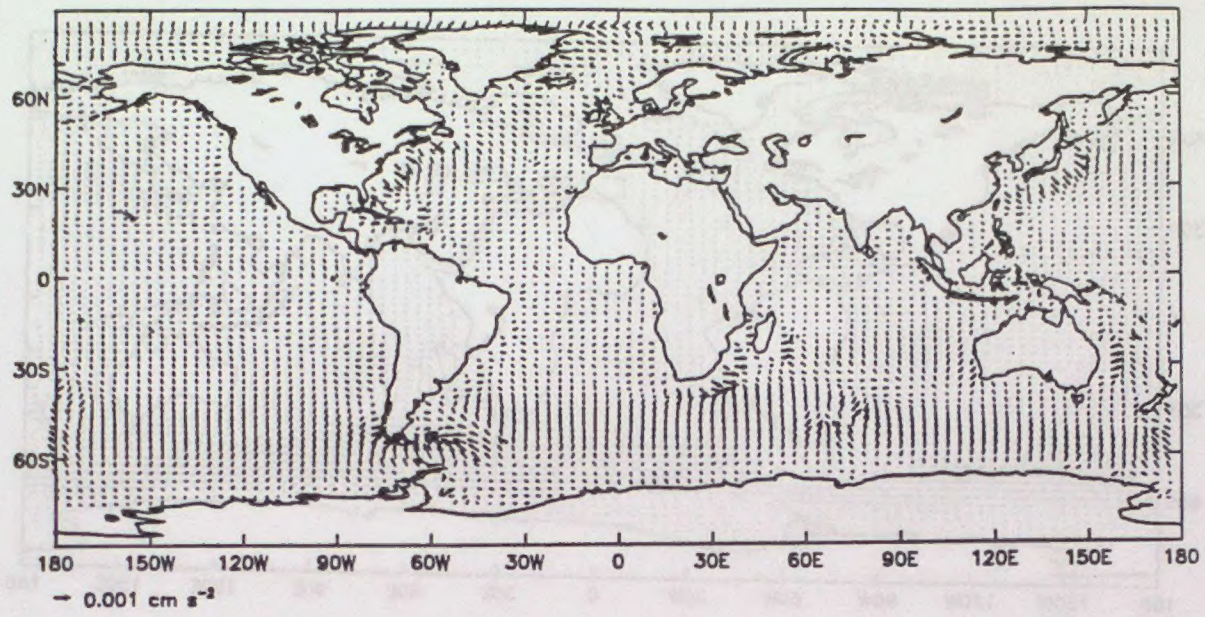

Figure 8: Depth-average baroclinic acceleration $\bar{\mathbf{a}}$

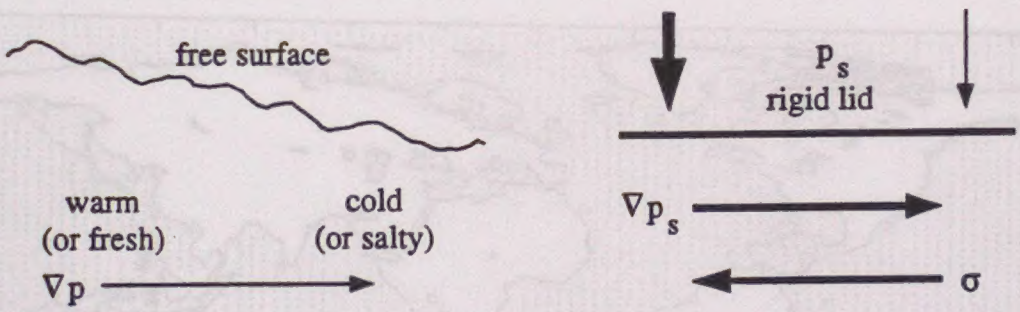

The horizontal hydrostatic pressure gradient ∇_{Hp} in the real ocean is represented in the model by the sum of two forces, namely the rigid-lid pressure gradient ∇_{Hp_s} and the hydrostatic pressure gradient σ resulting from the water column below the fixed surface only. These two forces are generally opposed and their individual depth- and area-averages are both considerably larger than that of their sum.

Figure 9: Interpretation of hydrostatic pressure gradient in the model

By comparison, the barotropic acceleration $\partial \bar{\mathbf{u}}_H/\partial t$ (not shown) has an average magnitude of $2{\cdot}92 \times 10^{-9}$ cm s^{-2}. In fact, at equilibrium, on the annual average, this term should vanish, because the stream function will not be changing.

We may write (6) and (4) in words as

$$\nabla_{Hp_s} = \bar{\mathbf{a}} - \text{barotropic} = -\text{advection} + \text{Coriolis} + \text{diffusion} - \text{hydrostatic} - \text{barotropic}.$$

Therefore the net pressure gradient

$$\nabla_{Hp} = \nabla_{Hp_s} + \text{hydrostatic} = -\text{advection} + \text{Coriolis} + \text{diffusion} - \text{barotropic}. \qquad (7)$$

We have seen that the vertical integral of σ is the largest component of the vertically integrated barotropic acceleration. Hence, obviously, the depth-average $\bar{\sigma}$ of this term is the dominant contribution to $\bar{\mathbf{a}}$, which itself is much larger than the barotropic part. Therefore we expect that the RHS of (7) to be small compared with either of the terms in the middle member, which will be of similar size and opposite sign, *i.e.* $\bar{\sigma}$ more or less balances ∇_{Hp_s}, which we take as representing the surface topography (see Figure 9). We would expect variations in surface height of 10 cm over distances of 1000 km, and hence a rigid-lid

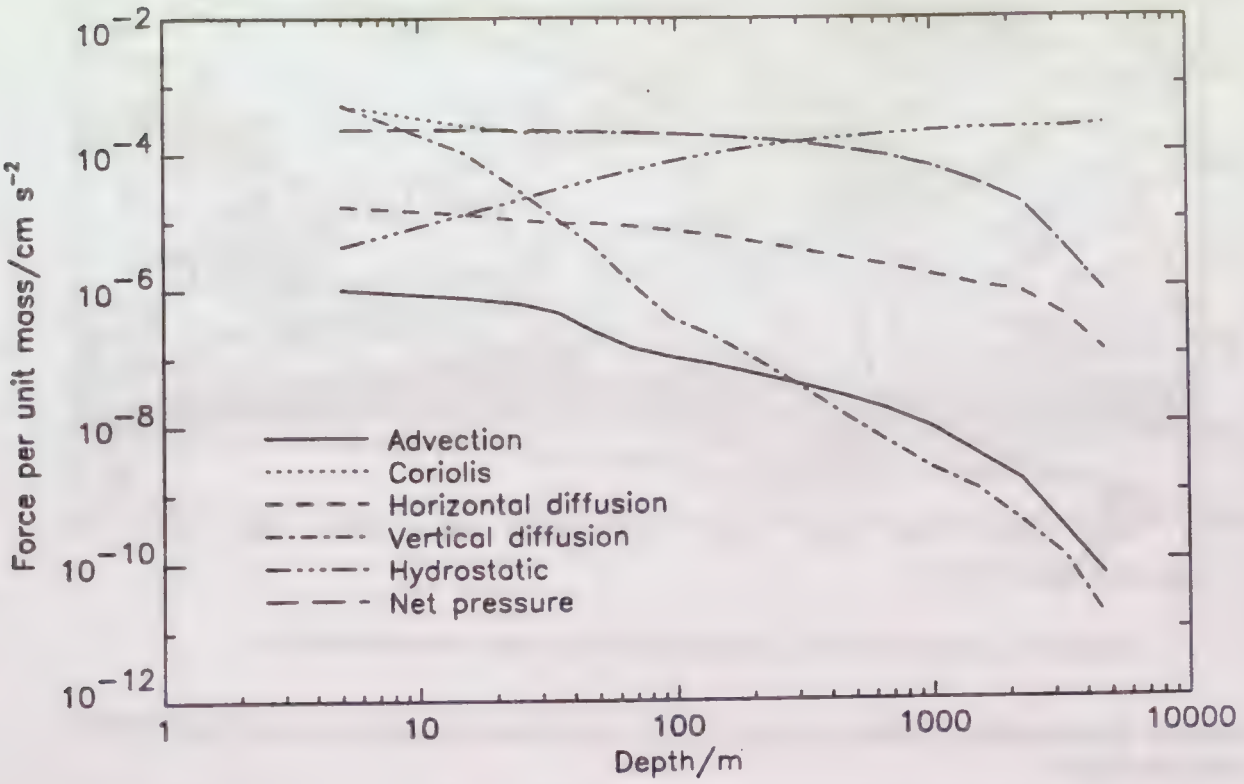

Figure 10: Depth profiles of various terms in the equation of motion in the control simulation

hydrostatic acceleration of $|\nabla_H p_s|/\rho = g|\nabla_H h| \simeq 10^3 \times 10 \div 10^8 = 10^{-4}$ (cm s^{-2}), or a depth-integral of $H|\nabla_H p_s|/\rho = 10^5 \times 10^{-4} = 10$ (cm^2 s^{-2}), which is indeed the observed magnitude of $|\int_{-H}^{0} \sigma \, dz|$.

When we evaluate $\nabla_H p/\rho$, we find that its depth- and area-average magnitude is $6{\cdot}21 \times 10^{-5}$ cm s^{-2}. This is exactly the same value as the average of the Coriolis term, the next largest of the contributions to $\nabla_H p_s$. That is, the net horizontal pressure gradient is balanced by the Coriolis force, the two also being oppositely directed. (A map of the former shows that it is the reverse of the latter.) This is the geostrophic balance. If the variation with depth of the magnitudes of the various terms is inspected (Figure 10), it will be seen that geostrophy holds accurately from level 3 (20–30 m) down to level 15 (1767–2677 m). The area-average σ increases with depth. This is unsurprising, because the hydrostatic pressure arises from the complete depth of water above a given level. (However, it need not be so, since there is no reason in principle why density gradients should not be in opposite directions at different levels, and thus cancel out at greater depths.) Then, since the same $\nabla_H p_s$ is transmitted to the bottom of the ocean, and is generally opposed to σ, $|\nabla_H p|$ decreases as depth increases. In the top layer, as noted above, there is an Ekman balance. Layer 2 is transitional. In the bottom two layers, the horizontal diffusion term becomes relatively larger. This could be because at these depths the ocean is divided into many small basins, leading to many boundaries at which large velocity gradients will be calculated.

The final result of this section is the p_s field obtained from $\nabla_H p_s$. This shown in Figure 11, where it has been converted to sea-surface height h in mm using the hydrostatic relation and assuming $\rho g \simeq 1025 \times 9{\cdot}81 \simeq 10^4$ Pa m^{-1}. (This value should be correct everywhere to within about 1%, given the actual range of surface seawater densities.) Since this is relative height field, its mean has been subtracted. The lowest sea-surface is $-1{\cdot}58$ m, off the coast of the Antarctic peninsular, and the highest is $0{\cdot}71$ m, near Madagascar. The area-weighted standard deviation is $0{\cdot}52$ m. The important features are: the strong slope across the Antarctic circumpolar current, from $-1{\cdot}2$ m around the coast to 0 m off Cape Horn, the Cape of Good Hope and southern Australia; and the summits at the eyes of the gyres towards the western sides of the Atlantic, Pacific and Indian ocean basins, near the Caribbean, Japan and Madagascar respectively. There seem to be few other maps of dynamic sea-surface with which this calculation may be compared, but two available ones are

- The control run of the Hamburg OGCM (Mikolajewicz *et al.*, 1990). This shows the same qualitative

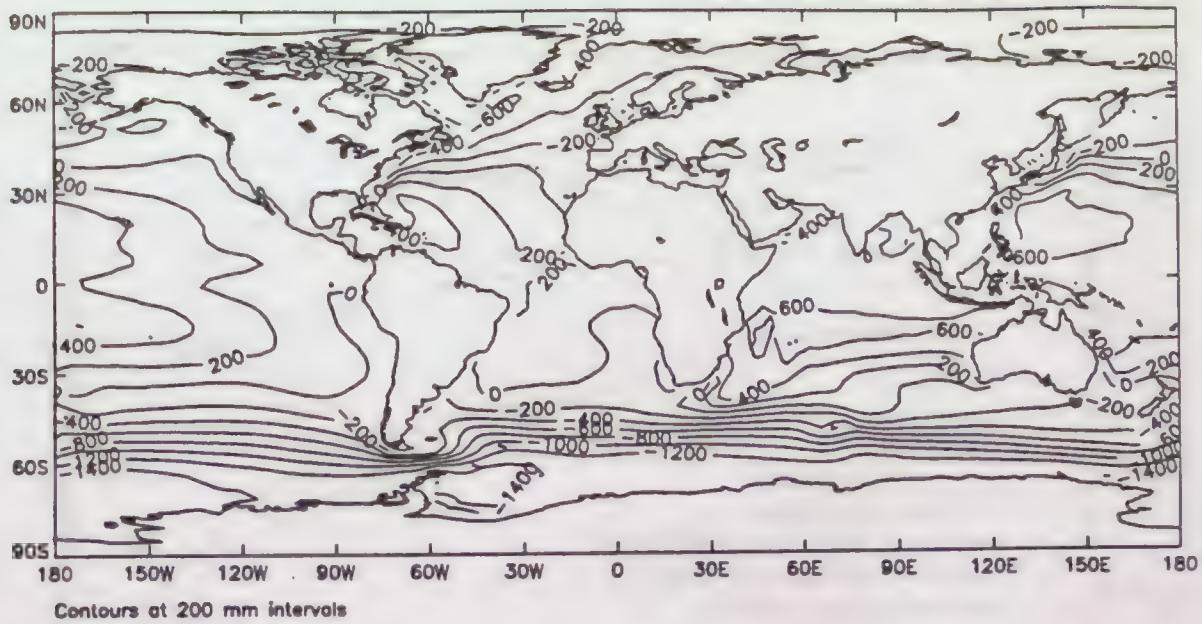

Figure 11: Relative sea-surface topography h from the control simulation

features. Quantitatively, it differs in that the north Atlantic and Indian oceans are about 0·4–0·6 m lower than ours.

- The observations for the Pacific of Wyrtki (1974). Both qualitatively and quantitatively this appears to be in good agreement with our calculation.

However, it should be remarked that, because the result is dominated by the hydrostatic term, if the model produces the correct sea-surface it may mean little more than that it has the right density structure. We return to this point in Section 5.

4 Differences between control and anomaly

To find change which has occurred in sea-surface topography by year y of the climate-change experiment, we diagnose h in both control and anomaly runs for this point, and compute

$$\text{(Anomaly, year } y\text{)} - \text{(Control, year } y\text{)}$$

(in what follows, we use Δ to indicate differences between the integrations in this sense). We use the control run in this way in order to subtract off the climate drift observed in that integration, as best we can, by assuming the same drift occurs in the anomaly integration, where its effect is combined linearly with that of climate change. As an illustration, we make this calculation for the end of the experiment, years 74–75. (Recall that we use two consecutive years for the calculation, in order to estimate $\partial\psi/\partial t$.)

In general, at all depths, the magnitudes of the *differences* in the various acceleration terms are between a quarter and a half of the magnitudes of those terms in the control. (The magnitude of the vector difference is not the same as the difference of the vector magnitude, because it takes into account changes in direction.) Evidently some fairly substantial changes in circulation occur. We can see what drives these by comparing the magnitudes of the various vector difference terms, shown in Figure 12. The conclusions from this, and from examining maps of the vectors, correspond to those we reached when analysing the control simulation: In the top layer, the change in the vertical diffusion term, which arises from the windstress, equals that in the Coriolis term, preserving the Ekman balance. In layers 3 and below, the change in the Coriolis term matches that in the *net* pressure gradient $\Delta\nabla_H p$, as required for geostrophic balance. With increasing depth, $|\Delta\sigma|$ rises and $|\Delta\nabla_H p|$ falls, since the same $\Delta\nabla_H p_s$ is felt at all depths. It is the last term which is related to the change in surface topography.

If we neglect the effect of change in windstress, what is happening can be described as follows. Changes in the density structure, consequent on alterations to temperature and pressure, give rise to changes in σ. This produces a change $\Delta\nabla_H p$ in the net pressure field, and the ocean circulation has to change in

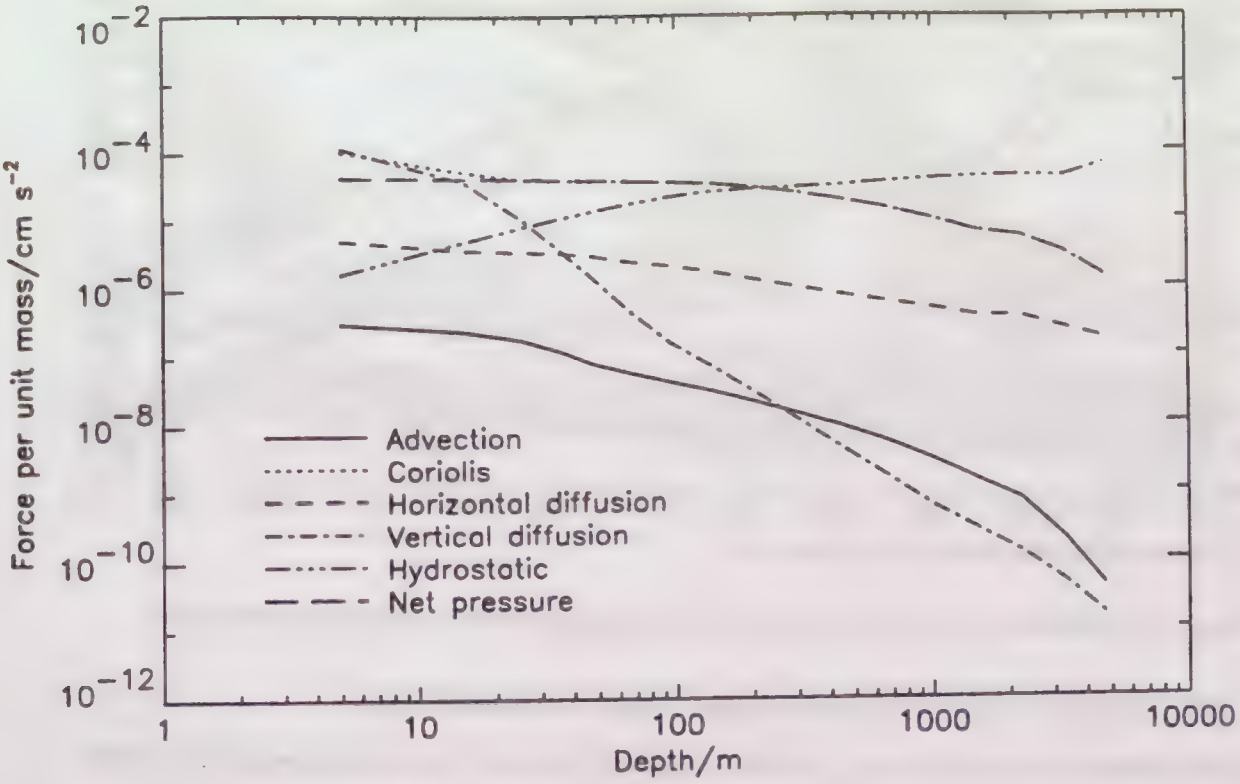

Figure 12: Depth profiles of various terms in the equation of motion, difference between initial and final states

order to adjust the Coriolis force and maintain the geostrophic balance. The new circulation implies a modified surface topography, and hence adjustments $\Delta\nabla_H p_s$ in surface pressure gradient, which tend to oppose $\Delta\sigma$. In the end, the new circulation is such that the change in the Coriolis force at each level balances the change in net pressure gradient.

Even though the depth-integrated velocity field is changing during the course of the experiment, $\Delta\partial\psi/\partial t$ is quite small. The depth- and area-average of $|\Delta a|$, the baroclinic term, is $4{\cdot}29\times10^{-5}$ cm s^{-2}; while the barotropic term $|\Delta\partial\bar{u}_H/\partial t|$ is $4{\cdot}28\times10^{-9}$ cm s^{-2}. The former is an order of magnitude smaller than the control value, the latter is twice the size of the control. Thus, the barotropic flow *is* changing. However, the rate of change is so small the ocean is nearly in equilibrium at all times.

The final result is Δh, computed by differencing h (not by inverting the vector acceleration differences). This is shown in Figure 13, in mm. As with the control simulation, this relative difference field has zero mean. Its minimum value is $-0{\cdot}16$ m, north of the Ross Sea, and its maximum is $0{\cdot}20$ m, to be found in Baffin Bay. There are notable rises in relative sea-level along the north-east coast of North America, presumably associated with the Gulf Stream, and in the western Indian Ocean. The results from the Hamburg experiment (Mikolajewicz *et al.*, 1990) could perhaps to be said to be qualitatively similar, in particular showing a fall in the Ross Sea and rises in the north Atlantic. In the next section we will relate this pattern of changes to that expected from the temperature structure alone. The standard deviation of Δh is 0·04 m, about an order of magnitude less than that of h in the control run, *i.e.* the alterations in the relative sea-surface topography are fairly small. Nonetheless, they are of the same order of magnitude as the global effect of thermal expansion, and it is therefore important to consider them if we are to obtain an accurate idea of local sea-level changes. It should also be noted that changes in surface atmospheric pressure will also influence local relative sea-level; however, in this experiment such changes are about an order of magnitude less, on average, than changes in rigid-lid pressure.

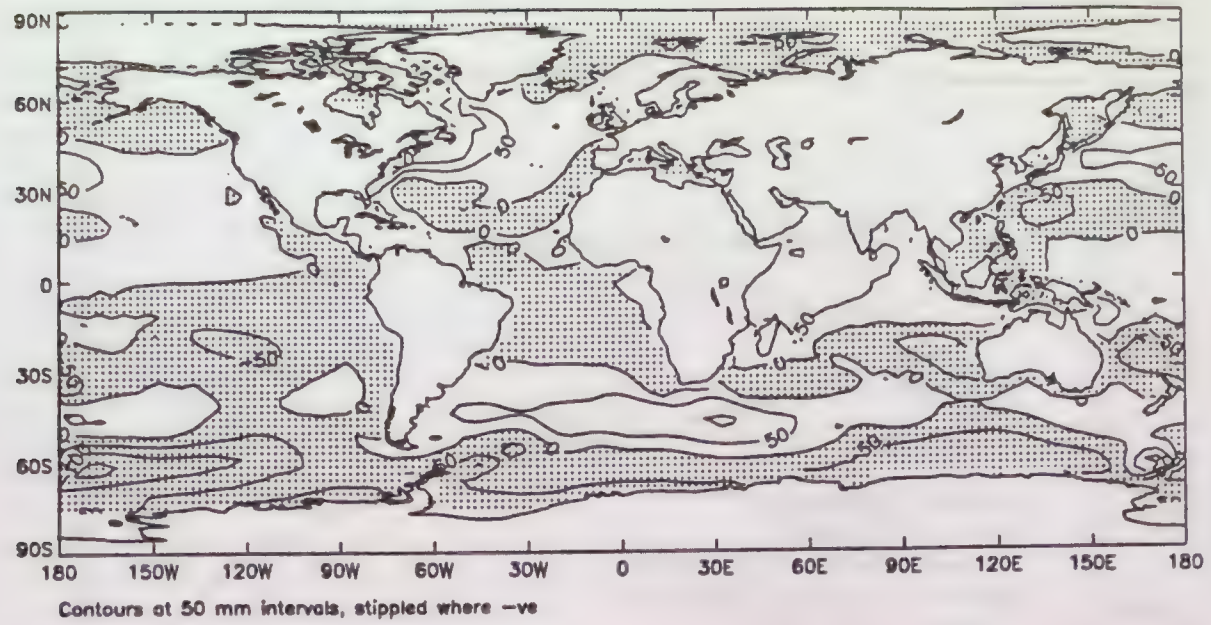

Figure 13: Differences Δh in relative sea-surface topography between initial and final states

5 Comparison of static and dynamical calculations

In doing this calculation, we have skirted round the question of whether it is really necessary. Is it possible to extract h and Δh directly from the 3D density structure of the ocean?

We can calculate the total mass of the model ocean,

$$M = \oint_A \int_{-H(x,y)}^{0} \rho \, dz \, dA. \tag{8}$$

where A is the horizontal sea-surface. It is clear that, since H is constant, M is not; *i.e.* the ocean model does not conserve water. It is possible for this to happen because of the form in which the continuity equation is used. Conservation of mass would require $\nabla \cdot (\rho \mathbf{u}) = 0$, but in the Boussinesq approximation the density is taken to be constant except in terms involving buoyancy forces. Hence continuity assumes the form $\nabla \cdot \mathbf{u} = 0$, which neglects the advection of density.

Since equation (8) is linear, the change in mass of the ocean between one state and another, in particular between corresponding years of the control and anomaly integrations, is

$$\Delta M = \oint_A \int_{-H}^{0} \Delta\rho \, dz \, dA.$$

However, we do not suppose that the mass of the real ocean will actually change greatly. What actually happens when the density structure of the ocean changes is that its volume V will alter. If ΔM is relatively small, we can use it to estimate the corresponding volume change of the real ocean as $\Delta V = -\Delta M/\rho$.

Since the extra volume ΔV is not represented in the model, in principle we have no information about how it is distributed. However, it seems sensible to assume that changes in local T lead to expansion and contraction more or less *in situ*. In that case, the appropriate density to use in computing ΔV is the local density, and

$$\Delta V = -\oint_A \int_{-H}^{0} \frac{\Delta\rho}{\rho} \, dz \, dA. \tag{9}$$

This suggests another way to state the requirement for the rigid-lid approximation to be valid, namely that the expansion of a given layer must be small compared with its thickness, so that the same vertical coordinate z is applicable to the layer in both states.

We have seen that, in the depth-average, the surface and hydrostatic pressure gradients are both much larger than the net pressure gradient. To a good approximation, then, we can set the RHS of (7) to zero, and obtain

$$\nabla_H p_s = -\bar{\sigma} = -\frac{1}{H} \int_{-H}^{0} \sigma \, dz = -\frac{g}{H} \int_{-H}^{0} \int_{z}^{0} \nabla_H \rho \, dz' \, dz, \tag{10}$$

referring to (2) for the definition of σ. This is telling us that $\nabla_H p_s$ is determined by $\bar{\sigma}$. Is $\bar{\sigma}$ significantly different from

$$\nabla_H \bar{p} = g \nabla_H \left\{ \frac{1}{H} \int_{-H}^{0} \int_{z}^{0} \rho \, \mathrm{d}z' \, \mathrm{d}z \right\},$$

the gradient of the depth-average hydrostatic pressure (*cf.* depth-average of the hydrostatic pressure gradient)? If $\bar{\sigma}$ could be replaced by $\nabla_H \bar{p}$, (10) would become $\nabla_H p_s = -\nabla_H \bar{p}$, *i.e.* we would have that $\nabla_H p_s$ equals the gradient of a scalar, and hence we would know p_s (to within a constant) immediately, without having to perform the numerical inversion. Operating with ∇_H on the expression in braces,

$$\nabla_H \bar{p} = -\frac{g}{H} (\nabla_H H) \bar{p} + \frac{g}{H} (\nabla_H H) \int_{-H}^{0} \rho \, \mathrm{d}z + \bar{\sigma}. \tag{11}$$

The first two terms contain the quantity $(\nabla_H H)/H$ multiplying, respectively, the depth-average and the bottom hydrostatic pressure, which might be expected to be of the same order of magnitude and different by a factor of around two (since density is roughly constant). $(\nabla_H H)/H$ is the effect of bottom topography, which is a field of steep gradients and large plateaux, and it turns out that the sum of the first two terms is about 10^4 times larger than the third term. $\nabla_H \bar{p}$ is therefore practically completely determined by bottom topography, rather than the surface topography through $\nabla_H p_s$. Thus, we cannot avoid the numerical inversion of p_s in order to obtain the surface topography.

Now we turn to the difference between experiments. The formulae are the same, with the replacement of pressures and densities by differences, since the terms we are concerned with are all linear. Hence, corresponding to (11),

$$\Delta \nabla_H \bar{p} = -\frac{g}{H} (\nabla_H H) \Delta \bar{p} + \frac{g}{H} (\nabla_H H) \int_{-H}^{0} \Delta\rho \, \mathrm{d}z + \frac{g}{H} \int_{-H}^{0} \int_{z}^{0} \Delta \nabla_H \rho \, \mathrm{d}z' \, \mathrm{d}z.$$

There is a crucial difference in this case, however, in that the density changes are mostly restricted to a layer near to the surface. Therefore the first and second terms, respectively proportional to the depth-average and bottom *change* in hydrostatic pressure, are of nearly equal size, since most of the water column experiences the effect of changes near to the surface. Thus these terms tend to cancel each other. In fact, a detailed calculation makes the average magnitude of their sum about five times smaller than that of the third term, which is itself about three times smaller than the average $|\bar{\sigma}|$ in the control run—this is as expected, because we noted that the range of h is greater than that of Δh by a similar factor. Hence, in the difference between initial and final climates,

$$\Delta \nabla_H \bar{p} \simeq \frac{g}{H} \int_{-H}^{0} \int_{z}^{0} \Delta \nabla_H \rho \, \mathrm{d}z' \, \mathrm{d}z = \Delta \bar{\sigma} = -\Delta \nabla_H p_s,$$

using (10), where we assume that only the hydrostatic term is of significance in the equations of motion. Therefore

$$\Delta \bar{p} = -\Delta p_s + \text{const} = -g \rho \Delta h + \text{const},$$

i.e. we can obtain the change in surface topography directly from the change in density structure.

Now

$$\Delta \bar{p} = g \Delta \left\{ \frac{1}{H} \int_{-H}^{0} \int_{z}^{0} \rho \, \mathrm{d}z' \, \mathrm{d}z \right\} \simeq g \int_{-H}^{0} \Delta\rho \, \mathrm{d}z$$

if the density changes are near to the surface, just as above, because throughout the majority of the water column, and hence in the depth-average, the entire change in hydrostatic pressure is experienced. Then by combining the last two equations we find that

$$\rho \Delta h \simeq -\int_{-H}^{0} \Delta\rho \, \mathrm{d}z + \text{const}.$$

Since ρ is nearly constant,

$$\Delta h + \text{const}. \simeq -\int_{-H}^{0} \frac{\Delta\rho}{\rho} \, \mathrm{d}z \equiv \Delta\eta.$$

This quantity appeared in equation 9; its area-average is the global-average sea-level rise if there are no salinity changes. It gives a good estimate of the changes in local relative topography, without the need for the numerical minimisation, provided that the hydrostatic pressure is the dominant term in the equation

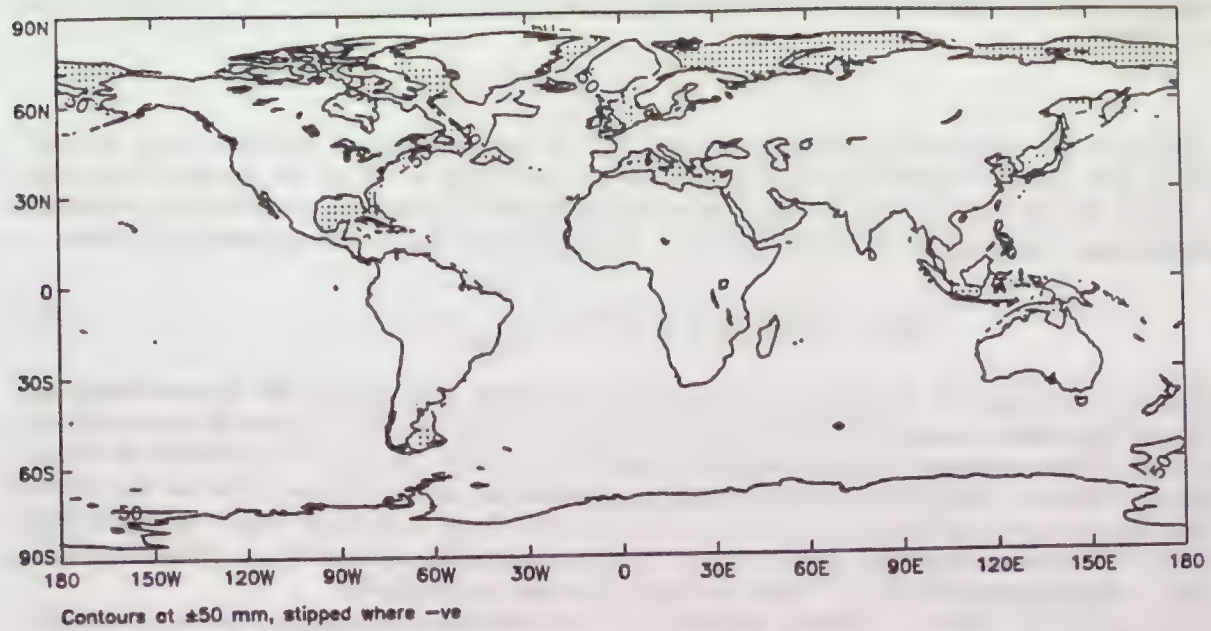

Figure 14: Relative difference between sea-level changes from the two methods, static – dynamical

of motion (which it is), and that the changes in density are restricted to a shallow layer. If the latter is the case, we can further replace $H(x,y)$ with a constant (and sufficiently large) H_0, and note that

$$\Delta\eta_0 = -\int_{-H_0}^{0} \frac{\Delta\rho}{\rho}\,dz$$

is in fact the change in dynamic topography relative to H_0 as a "level of no motion".

Calculating $\Delta\eta$ (and subtracting its area-average), we observe that it is mostly similar to Δh (which is computed with zero area-average). We refer to the former method as "static" and the latter as "dynamical". Their difference is exhibited in Figure 14. (The dynamical calculation is that made from years 74–75 together, while the static is the average of the results for the same two years.) It should be noted that this static calculation is *not* the same as the result of imposing an arbitrary warming on the ocean (the procedure of Church *et al.*, 1991). The temperature structure of the ocean, from which $\Delta\eta$ is computed, comes out of the model and is therefore dynamically adjusted. Over most of the ocean, the two methods give results differing by less than 50 mm. The most notable area of discrepancy is Baffin Bay and the Davis Strait, between Newfoundland and Greenland. In the Davis Strait, there is a strong (relative) sea-level rise from thermal expansion of over 400 mm, arising because there is a warming which extends to considerable depth; although the surface layer does not decrease in density very markedly, at 1000 m this region is exceptional. Therefore it is one where we might expect the static calculation to disagree with the dynamical, and indeed the latter gives a rise of around only 200 mm. In the dynamical calculation this same sea-level rise extends into Baffin Bay, but because the Bay is not as deep as the Strait, the static calculation shows a smaller change there, thus giving a discrepancy in the opposite sense between the two calculations, and a steep gradient between the Strait and the Bay in the $\Delta\eta$ field. In general, the Δh has weaker gradients than $\Delta\eta$, as indicated by the area-average values of $|\nabla_H \Delta h|$ and $|\nabla_H \Delta\eta|$.

6 Concluding remarks

The purpose of this note has been to explain and justify the method for calculating local relative sea-level changes from the rigid-lid ocean model. The discrepancies between this method and a calculation based on *in-situ* expansion indicate that to get an accurate picture of local sea-level change it is necessary to perform a dynamical calculation. This note does not discuss global-average sea-level rise, which is dealt with by Gregory (1993).

References

Church, J. A., Godfrey, J. S., Jackett, D. R. and McDougall, T. J. (1991) *A model of sea level rise caused by ocean thermal expansion*, J. Climate **4** 438–456

Cox, M. D. (1984) *A primitive equation, three dimensional model of the ocean*, GFDL Ocean Group Technical Report No. 1, GFDL, Princeton

Gregory, J. M. (1993) *Sea-level changes under increasing atmospheric CO_2 in a transient coupled ocean-atmosphere GCM experiment*, forthcoming in J. Climate

Mikolajewicz, U., Santer, B. D. and Maier-Reimer, E. (1990) *Ocean response to greenhouse warming*, Nature **345** 589–593

Murphy, J. M. (1992) *A prediction of the transient response of climate*, Meteorological Office Climate Research Technical Note 32

Numerical Algorithms Group (1990) *NAG Fortran Library, Mark 14*

Pacanowski, R. C. and Philander, S. G. (1981) *Parametrization of vertical mixing in numerical models of tropical oceans*, J. Phys. Oceanogr. **11** 1443–1451

Williams, G. P. (1972) *Friction term formulation and convective instability in a shallow atmosphere*, J. Atmos. Sci. **29** 870–876

Wyrtki, K. (1974) *The dynamic topography of the Pacific Ocean and its fluctuations*, Hawaii Institute of Geophysics, Report HIG-75-5

CLIMATE RESEARCH TECHNICAL NOTES

CRTN 1	Oct 1990	Estimates of the sensitivity of climate to vegetation changes using the Penman-Monteith equation. P R Rowntree
CRTN 2	Oct 1990	An ocean general circulation model of the Indian Ocean for hindcasting studies. D J Carrington
CRTN 3	Oct 1990	Simulation of the tropical diurnal cycle in a climate model. D P Rowell
CRTN 4	Oct 1990	Low frequency variability of the oceans. C K Folland, A Colman, D E Parker and A Bevan
CRTN 5	Dec 1990	A comparison of 11-level General Circulation Model Simulations with observations in the East Sahel. K Maskell
CRTN 6	Dec 1990	Climate Change Prediction. J F B Mitchell and Qing-cun Zeng
CRTN 7	Jan 1991	Deforestation of Amazonia - modelling the effects of albedo change. M F Mylne and P R Rowntree
CRTN 8	Jan 1991	The role of observations in climate prediction and research. D J Carson
CRTN 9	Mar 1991	The greenhouse effect and its likely consequences for climate change. D J Carson
CRTN 10	Apr 1991	Use of wind stresses from operational N.W.P. models to force an O.G.C.M. of the Indian Ocean. D J Carrington
CRTN 11	Jun 1991	A new daily Central England Temperature series, 1772-1991. D E Parker, T P Legg and C K Folland
CRTN 12	Jul 1991	Causes and predictability of Sahel rainfall variability. D P Rowell, C K Folland, K Maskell, J A Owen, M N Ward

CLIMATE RESEARCH TECHNICAL NOTES

CRTN 13	Jul 1991	Modelling changes in climate due to enhanced CO2, the role of atmospheric dynamics, cloud and moisture. C A Senior, J F B Mitchell, H Le Treut and Z-X Li
CRTN 14	Sep 1991	Sea temperature bucket models used to correct historical SST data in the Meteorological Office. C K Folland
CRTN 15	Aug 1991	Modelling climate change, and some potential effects on agriculture in the U.K. P R Rowntree, B A Callander and J Cochrane
CRTN 16	Aug 1991	The Boreal Forests and Climate G Thomas and P R Rowntree
CRTN 17	Aug 1991	Development of a Stratosphere-Troposphere Data Assimilation System. R Swinbank.
CRTN 18	Sep 1991	A study of asynchronous coupling using a simple climate model. M K Davey.
CRTN 19	Sep 1991	The Oceanic Carbon Cycle. N K Taylor
CRTN 20	Nov 1991	Worldwide ocean-atmosphere surface fields in Sahel wet and dry years using provisionally corrected surface wind data. M N Ward
CRTN 21	Dec 1991	Coupled tropical ocean global atmosphere models at the UKMO. M K Davey, C Gordon, S Ineson and S Lawrence
CRTN 22	Dec 1991	Empirical parameterisation of tropical ocean-atmosphere coupling. M Allen, M K Davey, D L T Anderson and P D Killworth
CRTN 23	Feb 1992	The temporal evolution of Equatorial Currents in the Indian Ocean D L T Anderson, D J Carrington, R A Corry and C Gordon
CRTN 24	Feb 1992	Stratospheric analyses provided by the U.K. Meteorological Office M J Bailey, A O'Neill and V D Pope

CLIMATE RESEARCH TECHNICAL NOTES

CRTN 25	Feb 1992	Modelling interannual variability in the Indian Ocean using momentum fluxes from the UKMO and ECMWF operational weather analyses. D L T Anderson and D J Carrington
CRTN 26	Mar 1992	A GCM simulation of the impact of Amazonian deforestation on climate using an improved canopy representation J Lean and P R Rowntree
CRTN 27	Mar 1992	The parameterization of rainfall interception in GCMs A J Dolman and D Gregory
CRTN 28	Jun 1992	Development of worldwide marine data eigenvectors since 1985 A W Colman
CRTN 29	Jun 1992	A tropical ocean model with reduced physics M K Davey
CRTN 30	Jun 1992	International Temperature Workshop, Boulder, Colorado, USA, 16 January 1992 Edited by D E Parker
CRTN 31	Jul 1992	Simulation of clear-sky outgoing longwave radiation over the oceans using operational analyses A Slingo and M J Webb
CRTN 32	Sep 1992	A prediction of the transient response of climate J M Murphy
CRTN 33	Nov 1992	LEPS scores for assessing climate model simulations and long-range forecasts. C K Folland
CRTN 34	Jan 1993	Stratospheric Data Assimilation System Guide Editer: R Swinbank
CRTN 35	Mar 1993	A Stratosphere-Troposphere Data Assimilation System R Swinbank and A O'Neill
CRTN 36	Mar 1993	Validation of hydrological schemes for climate models against catchment data. P R Rowntree and J Lean

CLIMATE RESEARCH TECHNICAL NOTES

CRTN 37	Apr 1993	Modelling of palaeoclimates: Examples from the recent past J F B Mitchell
CRTN 38	May 1993	A simulation of seasonality in ENSO forecast skill M K Davey, D L T Anderson and S Lawrence
CRTN 39	Jul 1993	ENSO Prediction experiments using a simpe ocean-atmosphere model D-H Wu, D L T Anderson and M K Davey
CRTN 40	Sep 1993	Diagnosis of dynamic sea-surface and sea-level changes from the Cox ocean model J M Gregory